Performance of practical beam-to-SHS column connections against progressive collapse

Wei Wang [a,b], Cheng Fang [b,*], Xi Qin [b], Yiyi Chen [a,b], Ling Li [b]

[a] State Key Laboratory of Disaster Reduction in Civil Engineering, Tongji University, Shanghai 200092, China
[b] Department of Structural Engineering, School of Civil Engineering, Tongji University, Shanghai 200092, China

ABSTRACT

This paper comprehensively discussed the performance of practical beam-to-SHS column connections against progressive collapse. Three full scale tests were performed on double-span systems subjected to the typical column loss scenario, where three connection types were covered in the test programme, namely, welded flange-weld web connection with internal diaphragms (specimen I-W), welded flange-bolted web connection with internal diaphragms (specimen I-WB), and welded flange-bolted web connection with short through diaphragms (specimen ST-WB). The test results, including failure modes/sequence, load–deformation responses and stress conditions, were presented in detail, and the load transfer mechanism over the entire loading process was thoroughly discussed. Comprehensive finite element (FE) models were then established to enable further discussion of the test results. Both experimental and FE results showed satisfactory ductility supply and load resistance of the three specimens, although specimen ST-WB exhibited the lowest ductility against initial fracture due to evident non-symmetrical stress distribution over the width of the beam flange. For the post-peak response, specimens I-WB and ST-WB showed reasonable regaining of the resisting load at later catenary stage due to a sufficient redistribution of the stress at the bolted shear tab connections, but limited post-peak load resistance was shown for specimen I-W which underwent quick propagation of the crack over the entire beam section. A simplified energy balance analysis showed that when a sudden column loss scenario is considered, progressive collapse may be triggered upon the initial fracture of the bottom beam flange of all the specimens.

© 2015 Elsevier Ltd. All rights reserved.

1. Introduction

Hollow sections are widely considered for structural column members due to their inherent architectural and structural advantages. The commonly used types of hollow sections include square, rectangular, and circular hollow sections (abbreviated as SHS, RHS, and CHS, respectively), whilst elliptical hollow sections (EHS) have also recently emerged as a structurally and aesthetically appealing solution [1]. Whilst the sound structural efficiency with good torsional stiffness make these hollow sections ideal for column members, some difficulties may exist associated with the practical detailing of the beam-to-column connections due to limited accessibility to the internal space of the closed section columns.

For hollow section columns with non-flat surfaces (e.g. CHS and EHS), outer diaphragms are usually welded around the column, and the adjacent open section (e.g. H-section) beams are connected

to the column via the diaphragms using either bolted or welded connections (or a combination of the two approaches). SHS/RHS may hold the benefit of their flat surfaces, where a more straight-forward connection detailing may be employed. In practice, the beam flange is normally connected to the column surface via welding, whilst the web of the beam is connected to the column through either direct welding or shear tab bolting. For both cases, as illustrated in Fig. 1(a) and (b), internal diaphragms (not shown in the figure), which are placed inside the column at the same elevations as those of the beam flanges, should be employed for strengthening purposes. It should be noted that this detailing leads to double-sided welding at the column wall (i.e. internal welding for the diaphragm plus external welding for the beam flange), which may influence the local performance of the SHS/RHS column, especially when the wall thickness is small. If the internal welding is not sufficiently strong (which may happen due to quality issues), separation between the internal diaphragm and column wall can occur when the connection rotates, and the tension flange of the beam can cause local fracture of the column wall [2]. In
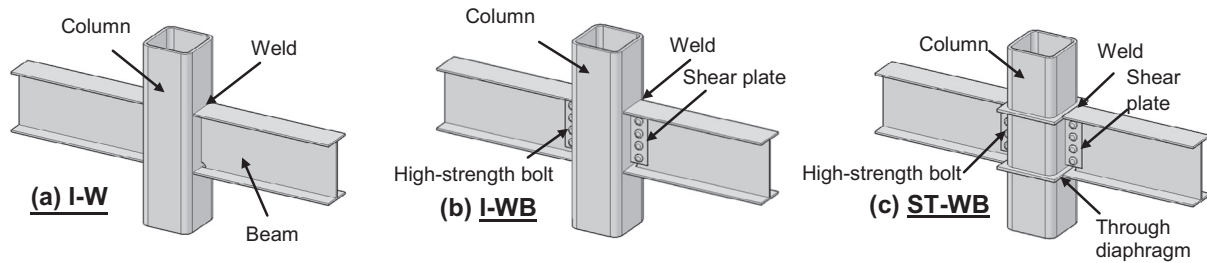
Fig. 1. Practical beam-to-SHS column connections.

addition, to facilitate internal welding (for the internal diaphragms), a stub column segment is usually prepared first, and after completing the weld work, the short column then needs to be welded to the remaining part of the column. This can further complicates the detailing of the connection, and importantly, causes more complex initial stress state of the column. An alternative solution is to use short 'through diaphragms' (i.e. continuous plates 'cutting' through the column), as shown in Fig. 1(c). In this case, the beam flange is directly welded to the edge of the diaphragm and the beam web can be bolted to the column with a normal shear tab connection. The use of the through diaphragms can be convenient for fabrication, where in practice, the steel tube is first cut into three pieces and then they are welded together with the two through diaphragms.

From the load transfer point of view, these beam-to-column connections are mainly subjected to bending and shear under normal conditions. When appropriately designed and fabricated, all the three solutions shown in Fig. 1 can be readily employed in practice and it seems that they have been serving the construction industry reasonably well over the past decade. However, there is sparse investigation into their performance when subjected to more complex loading states (e.g. combined axial force, bending, and shear) in conjunction with high ductility demand, and the lack of information may pose risk of unexpected failure when extreme loads occur. In particular, progressive collapse has been recognised as an essential design consideration, following several major accidents in the last century (e.g. Ronan Point apartment block and Murrah Federal building) [3]. The collapse of World Trade Centre in 2001 [4] brought the issue of structural robustness design back to the fore, and a global attention was then boosted. The design requirement against progressive collapse started to be introduced in design specifications and guidelines [5,6], and concurrently, significant research efforts have been devoted towards more comprehensive understanding of the progressive collapse mechanism for structures. For the performance of steel structures, which is the focus of the current study, intensive experimental work has been carried out at both sub-frame and full-frame levels [7–9], where idealised boundary conditions were normally considered for the former case to reflect the influence of the adjacent unaffected structures. Furthermore, as it has been well recognised that beam-to-column connections play a critical role in mitigating progressive collapse potentials, some studies focused on the connection performances under combined loading scenarios, where both rigid [10–14] and semi-rigid [15–19] connections have been studied in detail. Numerical investigations have also been performed to further examine the failure mechanism of structures/sub-structures [20,21], and in either the experimental or numerical work, the most widely used strategy is the alternative path method using the 'column loss' scenarios to simulate the consequence of blast, impact or fire [22,23]. In parallel, analytical models and practical design frameworks [24–26] have been emerging aiming to refine the existing design regulations.

However, most of the existing studies on structural progressive collapse have focused on steel frames with open section beam-to-open section column connections, whereas the robustness performance of those with practical beam-to-tubular column connections is still not well understood. Compared with the case of open section columns where bolted beam-to-column connections can be readily used, the behaviour of beam-to-hollow section column connections may be less easily predictable due to more complex connection detailing. With increasing popularity of the application of hollow section columns in modern construction [27], sufficient attention needs to be paid in terms of the robustness of such structural types to ensure public safety. This paper sheds considerable light on the fundamental progressive collapse performance of steel frames with beam-to-SHS column connections, where three full-scale sub-frame tests, covering the three practical connections types as shown in Fig. 1, are reported. The test results, including failure modes/sequences, load–deformation responses and stress conditions, are presented, and the load transfer mechanism along the entire loading process is thoroughly discussed. Comprehensive finite element (FE) models are then established to enable further interpretation of the test results, and design comments are finally outlined based on both experimental and FE results.

2. Experimental programme

2.1. Test specimens

Three test specimens, corresponding to the three typical connection configurations shown in Fig. 1, were considered in the current experimental programme. As the main variation was the connection detailing, the specimens were named as I-W, I-WB, and ST-WB for easy identification. These designations start with either 'I', which stands for internal diaphragm, or 'ST', which stands for short through diaphragm, and they end with either 'W' or 'WB', representing fully welded connection and welded flange-bolted web connection, respectively. Each specimen was mainly comprised of two H-section beams (H300 × 150 × 6 × 8 mm) and one short SHS column (250 × 14 mm) located at the mid-span, such that a typical sub-frame subjected to column loss scenario could be reflected. The geometric details of the test specimens are shown in Fig. 2(a). The overall length l_0 of the double-span sub-frame was 4.5 m, leading to a span-to-depth ratio of $l_0/H = 15.0$. The two ends of the system were vertically and horizontally constrained but were free to rotate (i.e. pin-supported). This boundary condition was considered to reasonably reflect the points of contra-flexures in real moment frames, as illustrated in Fig. 2(b).

Complete penetration groove welds were used to connect the beams and diaphragms to the column walls. The thickness of the internal diaphragms for specimens I-W and I-WB was the same as that for the beam flange (i.e. 8 mm), whilst for specimen
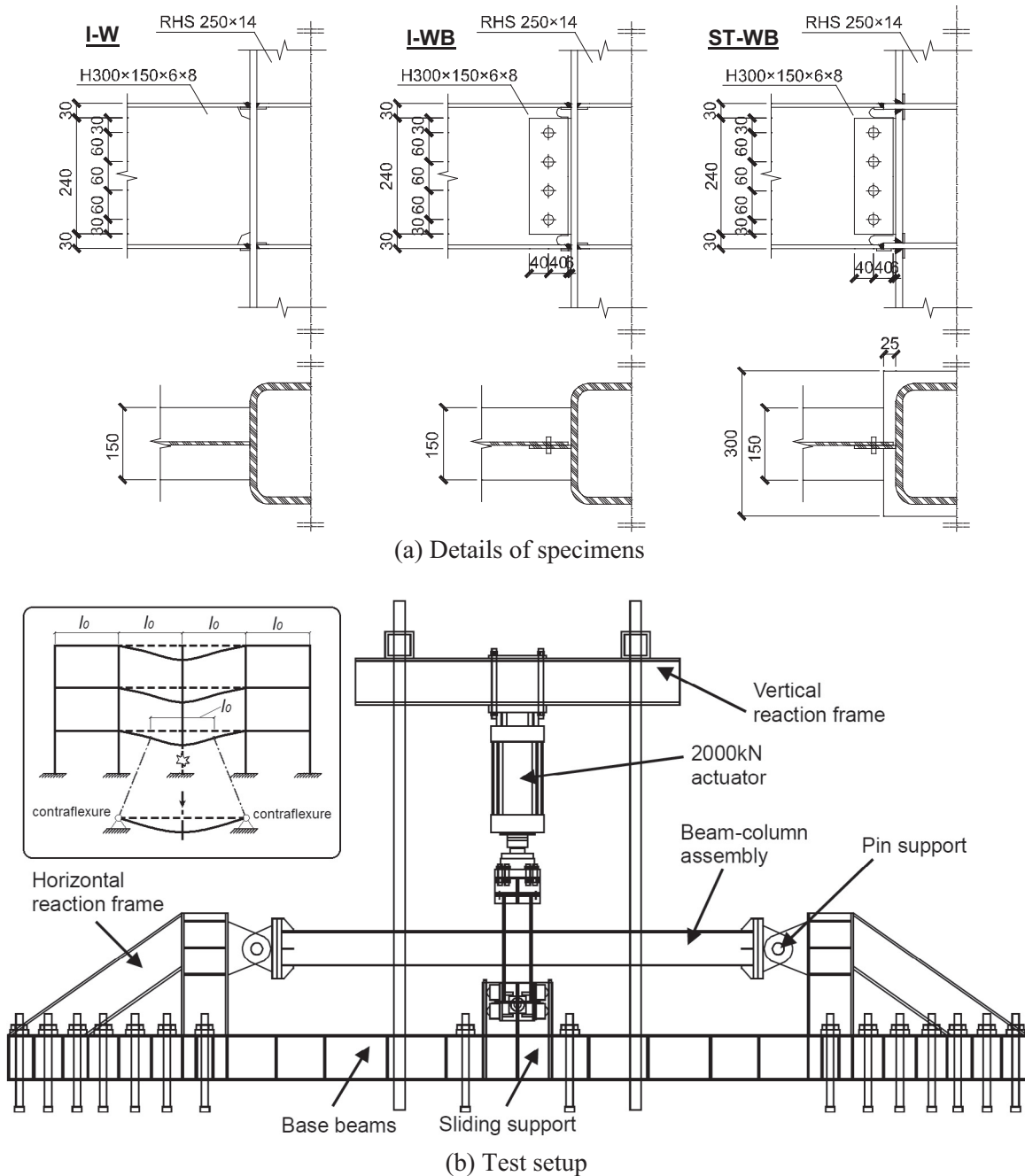
(a) Details of specimens

(b) Test setup

Fig. 2. Test arrangements.

ST-WB, 12 mm-thick through diaphragms were employed. For the bolted shear tab connections, four M20 Grade 10.9 frictional high-strength bolts were employed with a pre-tightening force of 155 kN [28]. The contact surfaces between the shear tab and the beam web were pre-treated with sand blasting. Grade S355 steel was considered for the specimens, and the detailed material properties were obtained via coupon tests according to the relevant specification [29], as detailed in Table 1. Each set of results in the table was based on the average values of three coupons for each part.

2.2. Test setup and procedure

The test setup, consisting of a servo actuator (capacity = 2000 kN), a column base sliding support, and self-balanced horizontal and vertical support frames, is schematically shown in

Fig. 2(b). A quasi-static point load was applied by the actuator to the top of the centre column with displacement control. During the loading process, the upper part of the column was fixed to the loading head, and the lower part was guided to move vertically through the sliding support, such that no rotational movement of the column was allowed. This led to a generally symmetrical performance of the system at the two sides of the column (i.e. 'east' and 'west' sides for ease of discussion), which is true when the column immediately above the affected floor can offer sufficient rotational restraints. In fact, minor gaps existed between the column and the sliding support, and therefore slight rotation can still be induced. The tests were terminated when either complete fracture of the connection occurred or the limiting displacement $\Delta_{\max}$ of the test frame was reached ($\Delta_{\max}$ was approximately 400 mm, corresponding to a beam chord rotation of 0.178 rad). For specimen I-W, however, malfunction of the column base sliding support

Table 1
Material properties from coupon tests.

Material	Yield strength (MPa)	Ultimate strength (MPa)	Rupture strain (%)	$(A_0 - A_{fracture})/A_0$
Beam flange (8 mm)	430	577	24	0.46
Beam web (6 mm)	417	514	27	0.48
Shear tab plate (6 mm)	409	505	29	0.61
Diaphragm (12 mm)	450	574	18	0.48
Column wall (14 mm)	482	545	24	0.68

Note: A_0 = original cross-sectional area of coupon, $A_{fracture}$ = necked cross-sectional area after fracture.

occurred during the test, and a certain level of column rotation was induced. In order to prevent damage to the actuator, the test stopped at a relatively early stage for this specimen when the displacement reached 200 mm. The two ends of the system were pin-supported via two hinges such that a full axial restraint was maintained. This was used to reflect the condition of relatively strong/rigid neighbouring sub-structures providing a sufficient level of axial restraints, which can be true for most typical steel frames due to the strong axial restraints offered by the adjacent beams in conjunction with the 'diaphragm effect' of the floor system [30]. The case of flexible adjacent structures, which leads to insufficient axial restraints to maintain catenary action of the affected double-span system, is not within the scope of the current discussion, and this may be worth future studies.

2.3. Instrumentations

The applied point load was automatically recorded by the actuator system, and the deflection of the double-span system was monitored through placing a series of displacement transducers along the beam length with certain intervals, as shown in Fig. 3 (a). Strain gauges were employed to monitor the strain distributions over critical beam sections, as generally shown in Fig. 3(b). For each specimen, the strains over the E1 and W1 sections (615 mm from the east and west beam end hinges respectively) were recorded to deduce the axial force development within the sub-frame, as discussed in detail in Section 4. The strains over the critical sections, i.e. sections E2/W2 and E3/W3, as illustrated in Fig. 3(b), were also recorded to examine the strain development conditions near the joint fractural zone.

3. Test results

3.1. General behaviour and failure modes

In general, all the specimens exhibited satisfactory load resisting capacity and ductility supply. No weld failure was observed, which indicated good weld quality for the specimens. The load–deflection responses of the three specimens, with the associated key failure stages identified during the loading process, are shown in Figs. 4–6. It should be noted that both the applied load F and the normalised load F/F_P are given in the figures, where F_P is the theoretical vertical resisting load corresponding to the formation of full plastic hinges of the beam at the critical sections W3/E3, under a flexural bending mechanism. In addition, both the displacement Δ and the beam chord rotation θ are given in the figures.

For specimen I-W, where the beam was fully welded to the column wall, linear load–displacement response was shown when the centre column displacement Δ was less than 30 mm. This indicated elastic flexural bending performance in the initial stage. F_P was achieved when Δ exceeded 60 mm ($\theta = 0.0\ 27$ rad), where local buckling was induced at the top flange of the beam, which may be attributed to combined effects of flexural bending and minor compressive arching. The resisting load kept increasing after

the occurrence of local buckling, and a peak load of 220 kN (point A1 in Fig. 4) was achieved at $\Delta = 142$ mm ($\theta = 0.0\ 63$ rad), at which moment fracture of the bottom flange at the W3 section occurred, leading to abrupt decreasing of the resisting load. The crack was initiated near the weld access hole, and then quickly propagated along the flange and web of the beam near the welds. In-plane rotation of the SHS column was then induced due to the malfunction of the column base sliding support, as discussed previously. The incline of the column caused a concentration of fracture at the W3 section, whereas no fracture was induced at the opposite side. With a further increase of the deflection, the column continued to incline, and the resisting load was maintained below 60 kN. To avoid damage to the loading system, the test was terminated at $\Delta = 200$ mm, where the crack had propagated to 1/3 depth of the beam web.

When the weld along the beam web was replaced by a shear tab bolted connection, as was the case for specimen I-WB, the failure behaviour could be evidently changed. As shown in Fig. 5, buckling of the top flange of the west side beam occurred at $\Delta = 75$ mm ($\theta = 0.0\ 33$ rad), and initial cracking was induced at the bottom flange of the W3 section near the weld access hole. When Δ achieved 166 mm ($\theta = 0.0\ 75$ rad), the crack propagated over the entire bottom flange, causing abrupt drop of the resisting load from 219 kN to 146 kN. After that, the resisting load started to pick up but the trend was quickly interrupted due to the subsequent fracture at the E3 section, where the resisting load dramatically dropped from 219 kN to 77 kN. With further increase of the deflection, the resisting load was slightly regained until the occurrence of fracture at the west side and east side shear tabs at $\Delta = 320$ mm and $\Delta = 387$ mm, respectively, during which stage the load–displacement curve showed evident fluctuation due to successive fractures along the bolt line. The W3 section experienced complete fracture at $\Delta = 400$ mm ($\theta = 0.178$ rad), and then the test was terminated.

For specimen ST-WB which employed short through diaphragms instead of internal diaphragms, top flange buckling was developed when the displacement reached 71 mm, and meanwhile minor cracking was induced at the bottom flange of the beam near section W3. The crack was initiated near the edge of the bottom flange at section W3, and it gradually propagated until complete fracture of the bottom flange when Δ reached 98 mm, and as a result the resisting load decreased from 154 kN to 100 kN. This was followed by an increase of the resisting load, which was accompanied by significant bearing deformation of the bolt holes of the shear tabs. Complete fracture of the bottom flange at section E3 occurred when $\Delta = 141$ mm, and as a result the resisting load dropped abruptly from 186 kN to 48 kN. Subsequently, gradual fracture of the shear tabs at both sides occurred whilst the resisting load kept increasing. Finally at $\Delta = 382$ mm ($\theta = 0.170$ rad), complete fracture of section W3 was induced, and the specimen completely lost its load resistance. It is worth mentioning that the peak resisting load immediately before the complete fracture of section W3 (i.e. point C5) exceeded the initial peaks (i.e. C1 and C2). This implies that at later stages, where the connections had already been severely damaged, a remarkable level of resisting load could
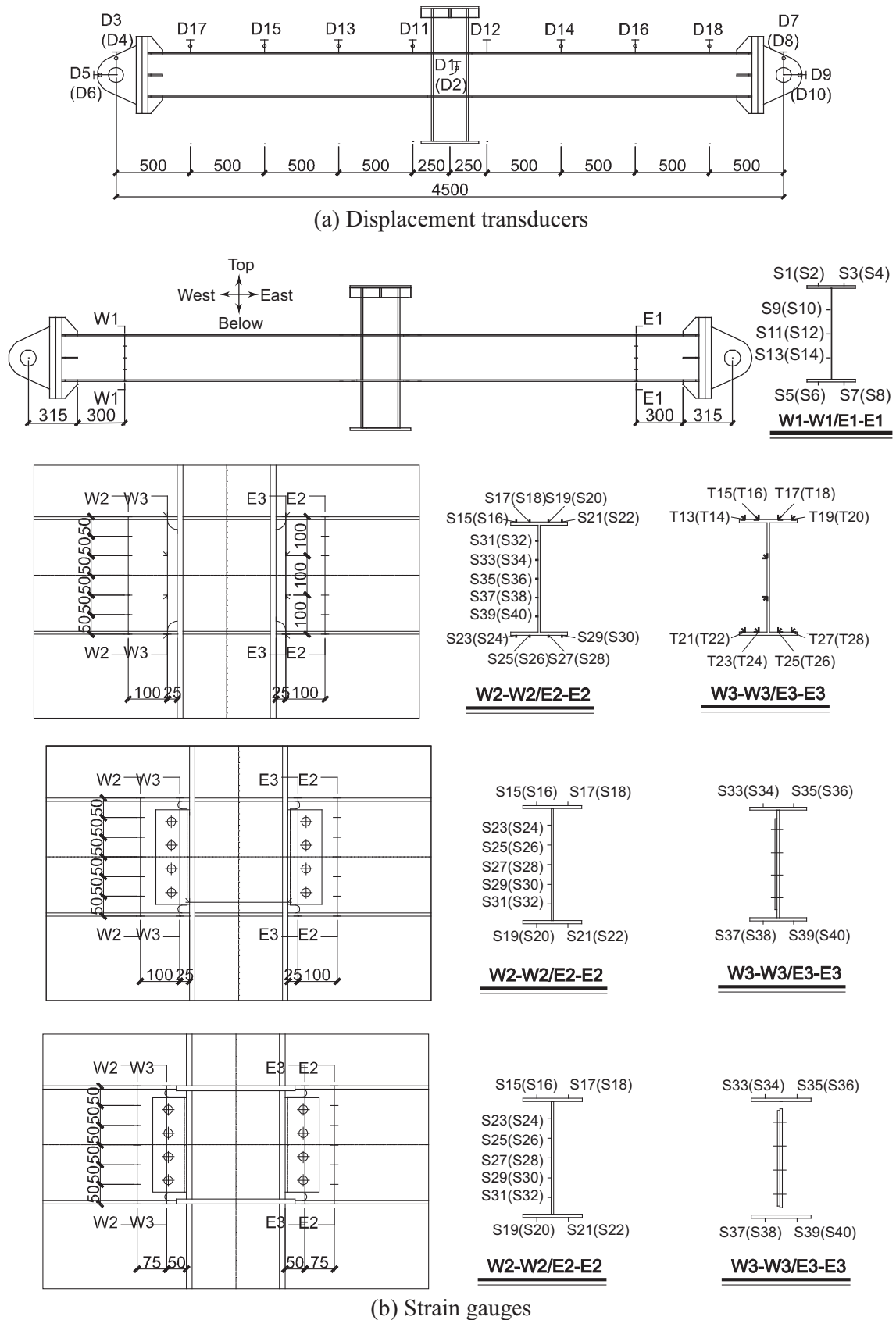
(a) Displacement transducers

(b) Strain gauges

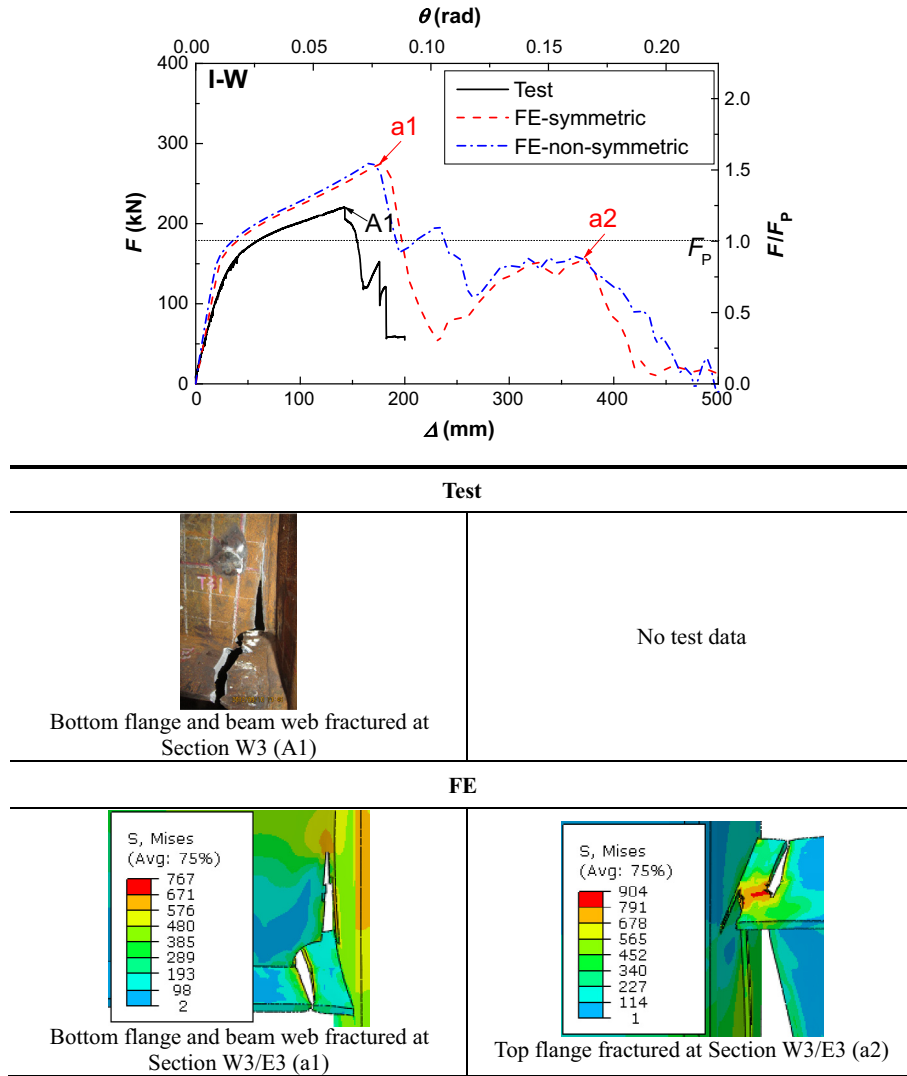**Fig. 3.** Test instrumentations.

Fig. 4. Test and FE results for specimen I-W.

still be maintained, which was probably attributed to the catenary action. This can be later confirmed by the axial force calculated from the strain distributions at sections E1/W1, as will be discussed in Section 4.

The load–deflection response of the specimens can be further depicted through the deflection profiles obtained from the displacement transducers placed along the length of the beams, as shown in Fig. 7(a). For specimens I-WB and ST-WB, because of the presence of the column base sliding support, the performance at the two sides of the column was generally symmetrical. For specimen I-W, however, the malfunction of the sliding support caused column rotation, and thus larger deflection was observed at the west side of the column due to localised development of cracking. Importantly, it can be seen that at initial loading stages, i.e. $\Delta < 30$ mm, a typical curved deformation shape was exhibited, which indicated that the resisting mechanism was mainly governed by flexural bending. With increasing deformations, the deformed configuration was gradually changed to that exhibiting two straight lines intersecting at the location of centre column, indicating that plastic hinges were developed near the connection zone. This reveals that the ductility demand of the specimen subjected to column removal was mainly accommodated by the connection zone, and the progressive collapse resistance of the

system was mainly dependent on the performance of these connections under complex internal forces.

3.2. Strain gauge readings

Typical strain gauge readings of the specimens are shown in Fig. 7(b). At the sections which were relatively far away from the connection zone (e.g. W1 section), typical bending action with top flange under compression and bottom flange under tension was shown at initial loading stages. With increasing deflection, the negative (compressive) strains started to convert to positive values, which indicated that the cross sections gradually turned from bending action to axial tension (i.e. catenary action). Some sudden changes of the strain gauge readings corresponded to the fracture of the connection zone (which caused decrease of the resisting load). No yielding was observed in the E1/W1 sections of the specimens, and therefore these strain gauge readings could be further used to calculate the axial force and bending moment of these sections. Much higher strain levels were observed at the critical sections in the connection zone (e.g. E2/W2 sections) due to considerable plastic deformation. Typical bending type strain distributions were shown in the initial loading stage, but the strains increased significantly when Δ exceeded 30 mm. The
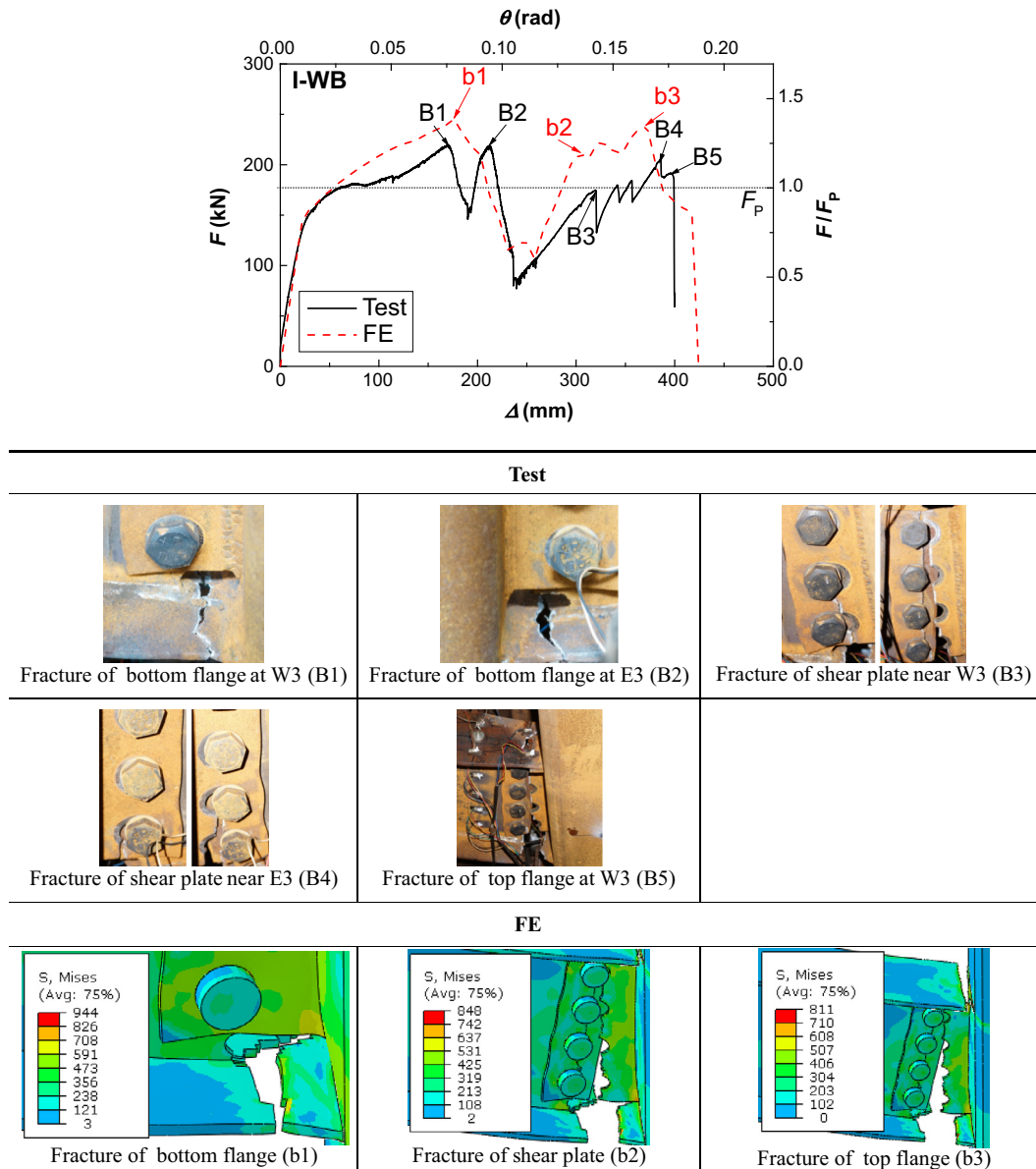
Fig. 5. Test and FE results for specimen I-WB.

strains at these sections showed less regular distribution patterns compared with those at E1/W1 sections, which was due to the more complex behaviour of the connection zones (e.g. local buckling and fracture of the beam). Most of the strain gauge readings over the height of the beam cross section exceeded the yield strain, which indicated that a plastic hinge was formed. At later loading stages, a transition trend from bending to bending–tension combined response was also shown, as signified by the gradual decrease of the negative strain.

4. Discussions of test results

4.1. Influence of connection detailing

The test results generally showed a similar level of ultimate load resistance (as listed in Table 2) for the three specimens. As it was observed that the initial fracture was developed at the bottom flange of the beam for all the specimens, the resisting load against initial fracture should be governed by the fractural strength of the bottom flange of the beam, provided that no premature weld failure occurred. Therefore, it was believed that the similar ultimate load resistance of the three specimens was attributed to the similar connecting method for the beam flanges to the column, i.e. by welding. It is of interest to find that although a similar level of resisting load upon initial fracture was observed, the fracture for specimen ST-WB was induced earlier than that for the other two specimens. This may be caused by the difference of the connection detailing near the bottom flange of the beam, noting that the beam flanges were directly welded to the column face for specimens I-W and I-WB, but they were welded to the edge of the short diaphragm for specimen ST-WB. The different configurations of the weld access holes may also attribute to the varying deflections where fracture of the beam bottom flange occurred.

After the initial fracture, the subsequent load resisting response differed evidently with different connection detailing. For specimen I-W, where the web of the beam was welded to the column face, the resisting load dropped significantly after the first load peak to a very low level with no sign of picking up until the end
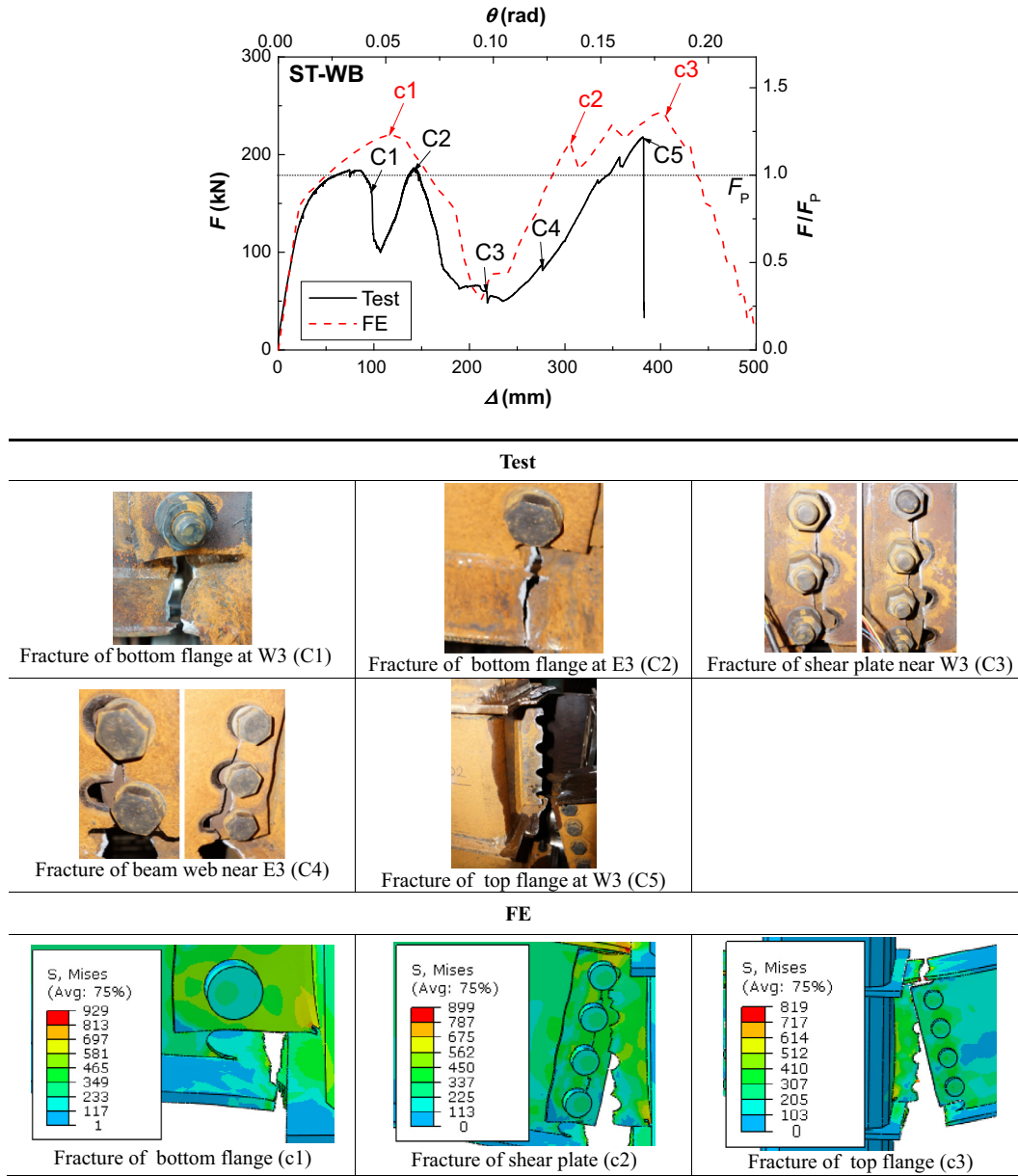
Fig. 6. Test and FE results for specimen ST-WB.

of the test, where 1/3 height of the beam web had been fractured. The low resisting load could be due to limited internal force redistribution capability of the specimen once the crack propagated to the web of the beam. Further numerical studies may be required to trace the load resistance conditions of the specimen at later stages. On the other hand, the internal force could be effectively transferred to the shear tab connections for specimens I-WB and ST-WB, and as a result a considerable portion of the loss of the resisting load could be regained during the redistribution of the force within the shear tab. This process could allow a further deflection of approximately 200 mm for the system with a reasonable level of resisting load sustained after initial beam flange fracture. During this process, the fractural strength of the shear tab was gradually exhausted, which finally led to complete fracture of the shear tab along the bolt line. This was quickly followed by the fracture of the top flange of the beam, leading to complete failure of the systems.

4.2. Load resistance mechanism

The load transfer mechanism of the specimens can be further interpreted through the internal forces developed within the subframe. As mentioned previously, the strain gauge readings in section E1/W1 can be employed to calculate the internal forces at the section, as given by:

$$N_1 = EA\frac{\Sigma\varepsilon}{n}, \ M_1 = EI\frac{\Delta\varepsilon}{\Delta h}, \ V_1 = \frac{M_1}{\sqrt{l_1^2 + \delta_1^2}} \tag{1}$$

where N_1, M_1 and V_1 are the axial force, bending moment and shear force at section E1/W1, respectively; E, A and I are the Young's modulus, cross-sectional area and second moment of area of the beam, respectively; $\Sigma\varepsilon/n$ is the average strain over the section; $\Delta\varepsilon/\Delta h$ represents the curvature of the section; l_1 is the horizontal distance between section E1/W1 to the pin-support; and δ_1 is the vertical
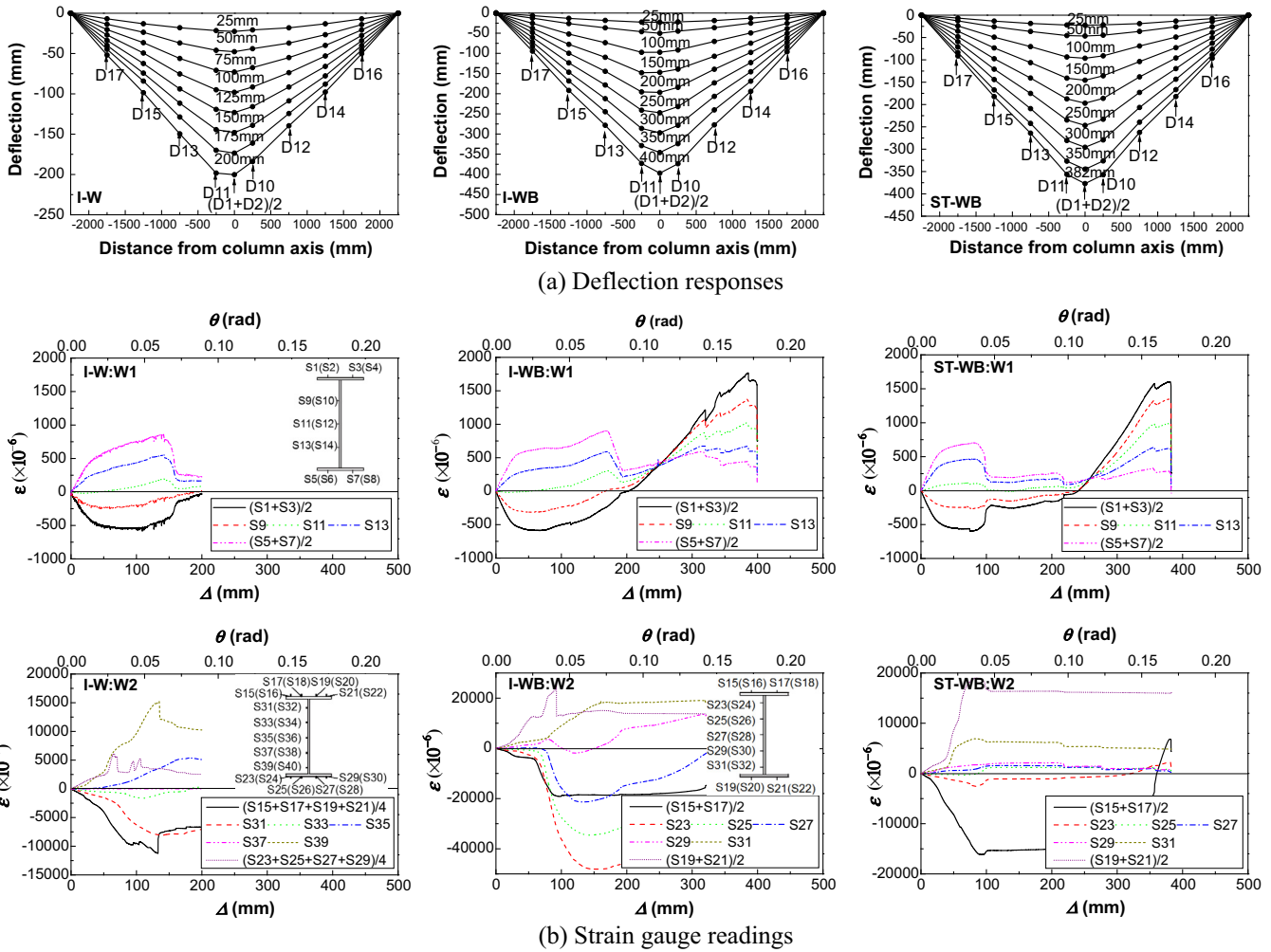
(a) Deflection responses

(b) Strain gauge readings

Fig. 7. Deflection and strain gauge readings.

Table 2
Results of experimental and FE studies.

Specimens	Test results				FE results				Connection type
	F_{IF} (kN)	Δ/θ at F_{IF} (mm/rad)	F_{FF} (kN)	Δ/θ at F_{FF} (mm/rad)	F_{IF} (kN)	Δ/θ at F_{IF} (mm/rad)	F_{FF} (kN)	Δ/θ at F_{FF} (mm/rad)	
I-W	220	142/0.063	–	–	273	176/0.078	155	375/0.167	Welded flange-welded web
I-WB	219	166/0.075	202	387/0.172	244	177/0.079	237	372/0.165	Welded flange-bolted web
ST-WB	184	84/0.038	218	382/0.170	220	118/0.052	242	399/0.177	Welded flange (via short diaphragm)-bolted web

Note: F_{IF} = load at initial fracture (initial peak), F_{FF} = load prior to final fracture.

deflection of the beam at section E1/W1 (according to the readings from the displacement transducers), as illustrated in Fig. 8(a). Based on the internal forces at section E1/W1, the vertical and horizontal reactions (V_R and H_R, respectively) of the pin support can be obtained:

$$V_R = V_1 \cos\theta_1 + N_1 \sin\theta_1, \ H_R = N_1 \cos\theta_1 - V_1 \sin\theta_1 \qquad (2)$$

where $\tan\theta_1 = \delta_1/l_1$. Considering the equilibrium of the beam segment, as shown in Fig. 8(a), the internal forces at any section can be obtained using the following expressions:

$$N_i = H_R \cos\theta_i + V_R \sin\theta_i, \ V_i = V_R \cos\theta_i - H_R \sin\theta_i, \ M_i = V_R l_i - H_R \delta_i$$
$$(3)$$

where i indicates the corresponding values (i.e. axial force, shear force or bending moment) at any section Ei/Wi. It should be noted

that the calculation of M_i is based on the assumption of non-fractured section, where the centroid is at the mid-depth of the beam. When fracture occurs, this calculated moment is inaccurate over the fractured section, and thus the result can only be considered as an indicative (or 'virtual') moment.

Based on the above equilibrium equations, Fig. 9(a) shows the calculation of the axial force at the critical section E3/W3 (where fracture occurred). It was observed that minor compressive force was induced at the very beginning, which was probably due to the compressive arching effect. As the double-span system was not overly 'stocky' with a reasonable l_0/H ratio of 15.0, the compressive force quickly decreased and tensile force was subsequently induced. The initial crack of the bottom flange of the beam led to decrease of the axial force, which echoes the load–deformation responses discussed previously. The axial force developed upon initial beam flange fracture could achieve $0.15N_p$
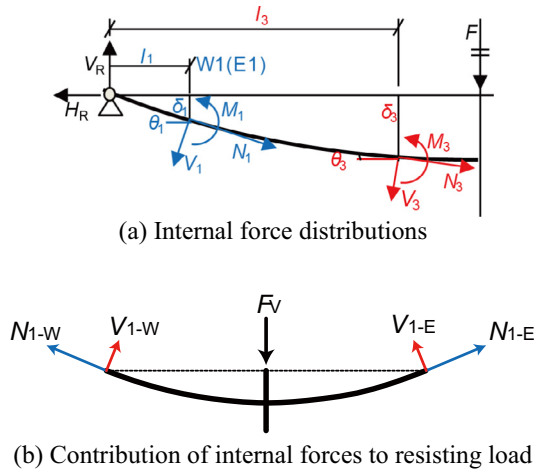
(a) Internal force distributions

(b) Contribution of internal forces to resisting load

Fig. 8. Free body diagram of test systems.

$(N_p = f_y A)$. Importantly, it can be clearly seen that after the inception of fracture, the axial force could still keep increasing for both specimens I-WB and ST-WB during the successive fracture of the shear tab connections, and prior to complete fracture of the entire

beam section, the maximum axial force could increase beyond $0.5N_p$. This confirmed that significant catenary action was developed at later stages of the loading process. For specimen I-W, the evolution of axial force could not be traced after the fracture of the beam flange due to early finish of the test, but it could be observed that no significant catenary action had been developed yet when the test was terminated.

Whilst the axial force continued to increase after fracture of the beam bottom flange, the flexural bending action showed an opposite trend, as shown in Fig. 9(b). At initial loading stages, the bending moment was developed following a typical flexural bending action, and the short plateau prior to the fracture of the beam flange was due to the significant plastic deformation induced at the critical sections, where plastic hinges could be formed (or nearly formed). After the occurrence of fracture, the bending moment decreased significantly, which indicated that the load resistance mechanism started to convert from flexural bending action into catenary action.

The load resistance mechanism can be further elaborated by illustrating the contributions from flexural bending action and catenary action to the overall resisting load. Based on the free body diagram shown in Fig. 8(b), the portion of the resisting load contributed to by the catenary action F_{R-C} can be expressed as:
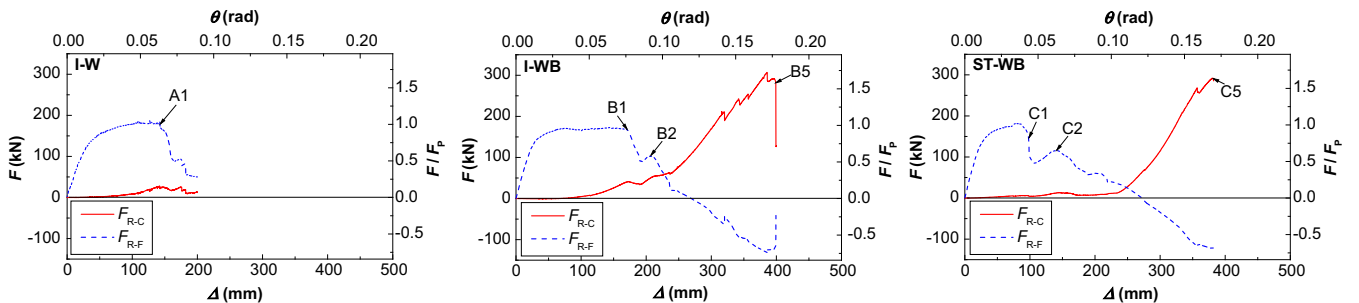
$$F_{R-C} = N_{1-E} \sin \theta_1 + N_{1-W} \sin \theta_1 \tag{4}$$
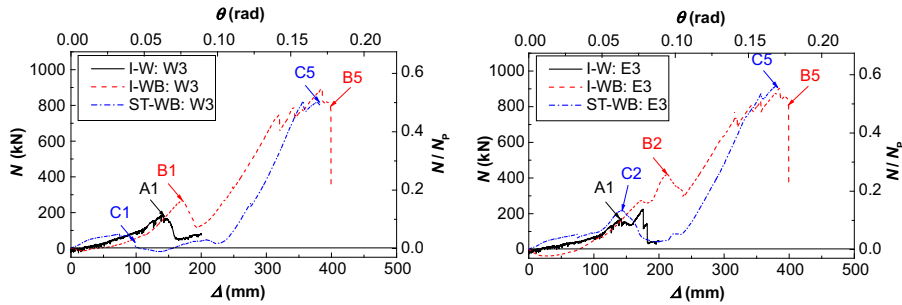
(a) Development of axial forces
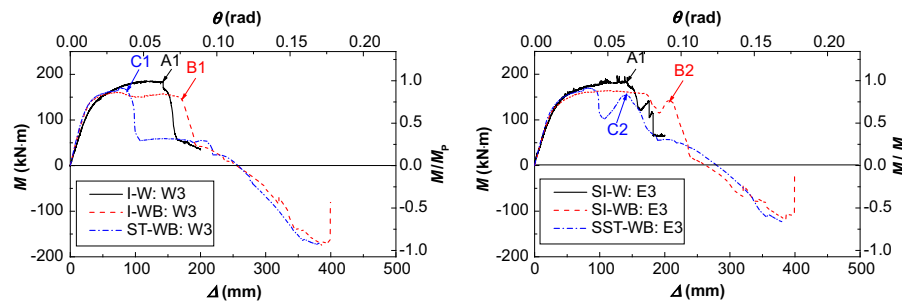
(b) Development of bending moment

(c) Contributions of internal forces to load resistance

Fig. 9. Load resistance mechanism.

and that contributed to by the flexural bending action F_{R-F} can be easily obtained by deducting F_{R-C} from the overall resisting load. Fig. 9(c) shows the contributions of the two actions to the resisting load, and the responses were in line with the previously discussed evolutions of the axial force and bending moment. The results confirmed that the load resistance of the specimens significantly relied on catenary action at large deflections, especially when Δ exceeded 200 mm.

4.3. Ductility supply

In practical design of building structures against progressive collapse, it is normally considered that the progressive collapse potential of a structure is governed by the ductility supply of the connections. The major design guidelines (e.g. DoD) stipulated a series of acceptable plastic rotation angles (Acceptance Criteria) for various connection types for nonlinear modelling of steel connections, and failure may be considered to occur if the plastic rotation angles of the connection exceeds the acceptable ones. In particular, if a connection exhibits an idealised multi-linear curve type as shown in Fig. 10(a) (which is the case for the current specimens), detailed acceptable plastic rotation angles (i.e. limiting values of 'a' and 'b') are listed [6]: for welded unreinforced flange-bolted web connections (i.e. specimens I-WB and ST-WB), the acceptable plastic rotation angles (in radian) are $a = 0.021 - 0.0118d = 0.017$ and $b = 0.050 - 0.0236d = 0.043$, where d is the beam depth in metre. For welded unreinforced flange-welded web connections (i.e. specimens I-W), the values may be taken as $a = 0.0284 - 0.0157d = 0.024$ and $b = 0.043 - 0.0236d = 0.036$. In addition, the acceptable residual strength ratio c, which is expressed as the ratio of the post-fracture resisting load

over the initial peak load, is taken as 0.2. Following the design guidelines, the load vs. beam chord rotation responses of the three specimens can be idealised by multi-linear curves as shown in Fig. 10(a). The plastic rotations can be obtained by deducting the yield rotation θ_y from the overall beam chord rotation. In general, all the three specimens showed sound ductility when subjected to mid-column removal. The plastic rotation angle a (i.e. that prior to initial fracture) ranged from 0.031 to 0.065 rad, which significantly exceeded the acceptance criterion proposed by DoD [6]. This indicates that all the three practical beam-to-SHS column connections can accommodate significant plastic rotation without loss of resisting load. For the post-peak response, the plastic rotation angles b for specimens I-WB and ST-WB were evidently larger than those stipulated in DoD [6]. The minimum residual strength ratio c of the specimens was 0.251, which exceeded the acceptance criterion of 0.2. The results generally showed that the recommended acceptance criteria for ductility performance of fully restrained moment connections are on the conservative side for the current specimens.

4.4. Prediction of dynamic response

The focus of the current experimental study was given to the static performance of the double-span systems subjected to centre column loss, but when actual extreme events occur (e.g. blast), sudden column removal, which is associated with dynamic response, can be a more rational assumption that realistically reflects the consequence of an extreme event. Sudden removal of a column is in effect close to suddenly applying the gravity load on the same structure in the absence of the column at the beginning, especially when significant displacements can be sustained
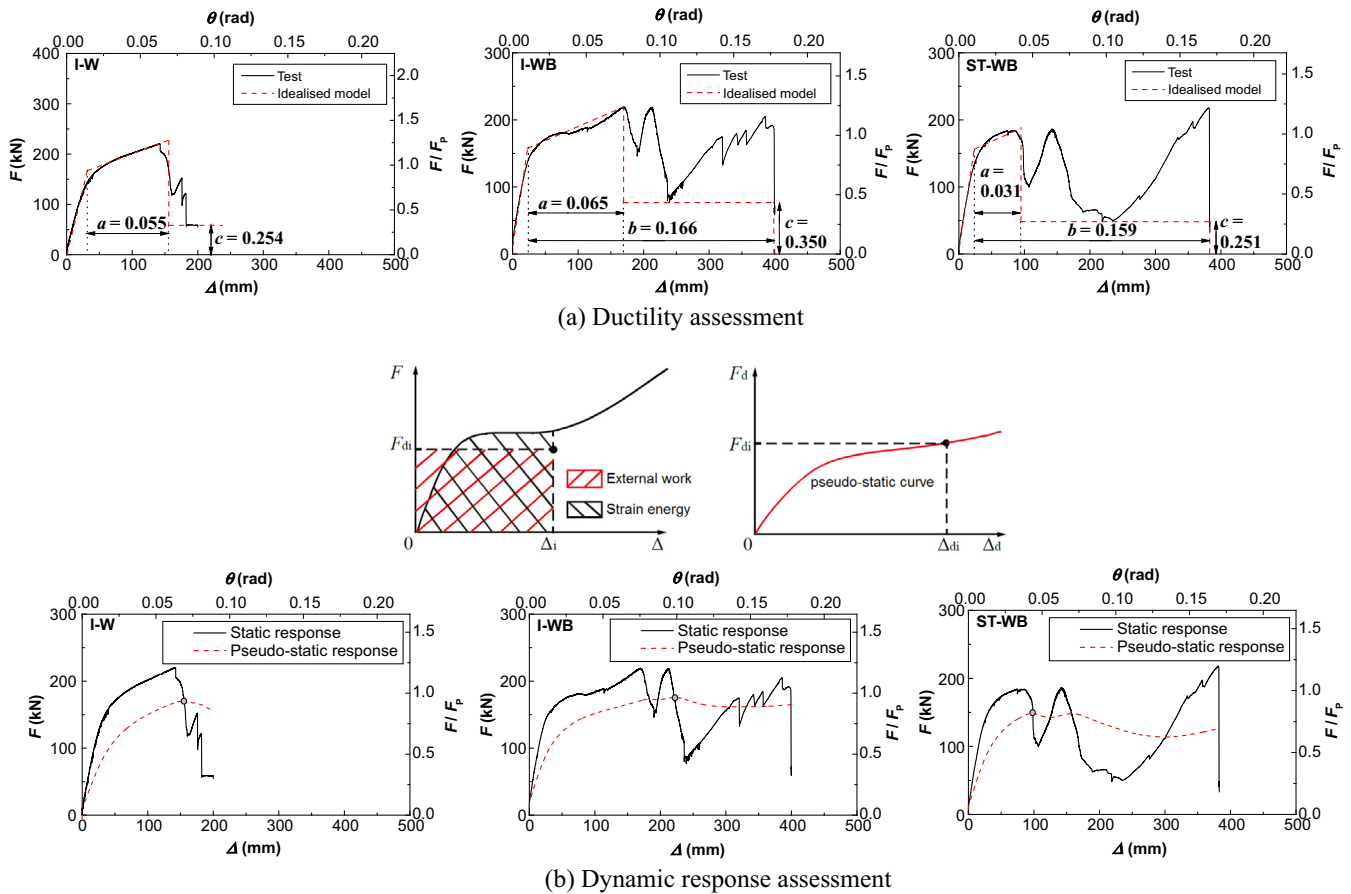

(a) Ductility assessment

(b) Dynamic response assessment

Fig. 10. Further discussion of test results.

by the structure as a result [24]. Based on the available static response, such as the static load–deflection response obtained from the current study, a dynamic response reflecting sudden column loss can be deduced using an energy balance approach proposed by Izzuddin et al. [24]. An important benefit of this method is its convenience of using the principle of energy balance to perform simplified dynamic assessment instead of directly conducting complex nonlinear dynamic analysis. As illustrated in Fig. 10(b), if the static load–deformation response is known, the allowable dynamic (i.e. sudden column loss) load resistance at any ductility demand can be obtained by achieving an equivalence between external work and internal energy, i.e. when the two hatched areas become identical. By considering different levels of ductility demand and employing the energy balance principle, a dynamic (pseudo-static) curve, which represents the relationship between the sudden applied load and the associated dynamic deformation, can be constructed.

Fig. 10(b) shows the pseudo-static load vs. central column displacement responses based on the available static test results. It is generally observed that at the same applied load, the ductility demand of the system subjected to sudden column loss is evidently higher than that with static column removal. In other words, with the same ductility demand, the allowable resisting load to prevent progressive collapse is decreased if the system experiences sudden column loss. A gradual decrease of the pseudo-static curve is shown after reaching the maximum load capacity, which indicates that if the applied load exceeds the maximum dynamic load capacity marked in the figure, the internal energy stored within the deformed system cannot balance the external work done by the applied load again (even though significant regain of the static resisting load is exhibited), and progressive collapse can hence be triggered as a result. Despite this, the regain of the static resisting load after initial fracture still tends to slow the decreasing rate of the pseudo-static curve, and it is believed that if a further pick up of the static resisting load can be developed beyond that observed in the current specimens, the strain energy stored over this regaining process can finally re-balance the external work, and the equivalent state will be achieved at a much larger deformation with larger load resisting capacity. Since no such significant regain of the static resisting load was developed for the three specimens tested in this study, it may be preliminarily concluded that, when a sudden column loss scenario is considered, progressive collapse may be triggered upon the initial fracture of the bottom flange of the beam. This can be preliminarily considered as a simplified and conservative failure criterion for such connections in practical design when sudden column loss strategy is incorporated.

5. Numerical study and further discussion

5.1. Modelling strategy

As the early finish of the test for specimen I-W prohibited a complete understanding of its load resistance mechanism, the development of numerical modelling can offer an efficient complementary insight into its progressive collapse performance at later loading stages. The numerical study can also effectively reveal the complex stress distributions within the structural components, which may help explain the fracture initiation and propagation phenomena of the three specimens. The general nonlinear finite element (FE) analysis package ABAQUS [31] was used for this purpose. As the current numerical study involves complex material behaviour (e.g. fracture) and a large number of contact pairs, convergence difficulty could be a critical issue. This can be addressed by employing the dynamic explicit analysis which is able to well predict the quasi-static response of structures with negligible dynamic effect, if the kinetic energy of the deformed structure is sufficiently low compared with its internal energy. Therefore, by ensuring that the kinetic energy was kept within 10% of the internal energy throughout the entire simulation process, as suggested by [32], explicit solver was used for the current numerical analyse.

The C3D8R elements, which are 8-node linear brick elements with reduced integration and hourglass control, were employed for all the structural components, including the SHS column, H beam, diaphragm plates, shear tab, and high-strength bolts. The general meshing size for the column and beams was approximately 5 mm, but a refined meshing size of around 1 mm was employed for the areas adjacent to the connection zone, as typically shown in Fig. 11. 'Hard contact' with no penetration in the normal direction was considered for all contact pairs, and a coefficient of friction of 0.45 was used corresponding to the actual treatment of the steel surface. As no weld failure was observed during the tests, the 'tie' interactions were employed to simulate all the complete penetration groove welds. The boundary conditions of the models were applied to reflect the actual conditions of the test setup, where idealised pin-supports were considered at the two external ends of the beam and the centre column was only allowed to move vertically with no in-plane rotation. For specimen I-W, however, two boundary conditions for the centre column were considered: (1) the column was laterally restrained along the length, which is consistent with the boundary condition for the other two specimens, and (2) the constraints at the lower part of the column was removed, which was used to consider the actual case where the column base sliding guide did not work properly for this specimen. For the latter case, the material fractural strain (as discussed below) of the beam at one side of the column (east side) was slightly increased in order to trigger non-symmetrical performance (e.g. fractural development) of the symmetrical FE model.

The basic nonlinear material property of steel was simulated using the isotropic hardening model with the von Mises yield criterion. The fundamental material properties, including the modulus of elasticity, yield strength, and ultimate strength, were obtained from the tensile coupon test results. The engineering stress σ_{Eng} and strain ε_{Eng} were then converted to true stress σ_T and strain ε_T in ABAQUS, as expressed by:

$$\sigma_T = \sigma_{Eng}(1 + \varepsilon_{Eng}), \ \varepsilon_T = \ln(1 + \varepsilon_{Eng}) \tag{5}$$
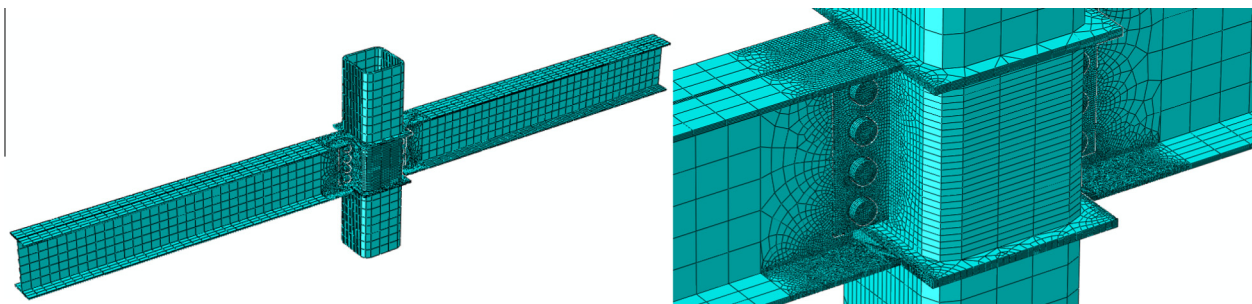

Fig. 11. Typical finite element model and meshing scheme.

and the true plastic strain ε_p for ABAQUS input can be obtained by:

$$\varepsilon_p = \varepsilon_T - \frac{\sigma_T}{E} \tag{6}$$

To simulate fracture of steel, the progressive ductile damage model offered by ABAQUS was employed. The damage model allows for ductile fracture of steel that experiences extensive plastic deformation in the necking phase prior to fracture, and after the initiation of fracture, a user-defined degradation response of the material stiffness is enabled, where the fully damaged elements will be deleted from the mesh. Therefore, in order to capture the progress of material damage, two sets of parameters need to be incorporated, namely, a damage initiation criterion and a damage evolution response. The damage initiation criterion describes the maximum equivalent plastic strain which initiates damage. The damage evolution law describes the condition of degradation of the material stiffness once the corresponding initiation criterion has been reached, and a linear damage evolution law was considered in the current study.

To simulate the fracture of steel under a uniaxial state, the failure true stress σ_f and strain ε_f (at which fracture is triggered) can be obtained from the coupon test results and by using the following equations:

$$\sigma_f = \frac{F_{\text{fracture}}}{A_{\text{fracture}}}, \quad \varepsilon_f = \ln\left(\frac{A_0}{A_{\text{fracture}}}\right) \tag{7}$$

where F_{fracture} and A_{fracture} are the tensile load and the necked (reduced) cross-sectional area of the coupons where fracture occurred, and A_0 is the original cross-sectional area of the coupons. When the material is subjected to multi-axial stress states, the influence of stress triaxiality on the material fractural behaviour may need to be considered. However, as detailed triaxial material testing is normally not considered as a standard procedure in common experimental programmes, and metal fracture itself is a complicated issue, inconsistent approaches were normally employed in various investigations [2,10,32–34]. Some studies adopted an iterative procedure to determine the input parameters for fracture simulation [2,10]. In this study, a simplified approach based on 'Rupture Index (RI)' [34] was used to reflect stress triaxiality, as given by:

$$RI = \frac{PEEQ}{e^{-1.5T}} \tag{8}$$

where PEEQ is the equivalent plastic strain, T is the stress triaxiality which is the ratio of the hydrostatic stress over the von Mises stress. Rupture Index is an indicator reflecting the potential for ductile fracture (i.e. the higher the PEEQ, the higher the potential for fracture), and the value at fracture for a specific material may be obtained by using Eq. (8) with the uniaxial coupon test results, where $T = 0.33$ for the uniaxial loading state. Employing a consistent Rupture Index for the same material, the plastic fracture strain (the PEEQ value that causes fracture) at various stress triaxiality conditions (i.e. various T values) can be obtained. These plastic fracture strain and stress triaxiality (T) pairs were then directly input into ABAQUS for simulation of steel fracture at various stress states. It should be noted that this is only a convenient and simplified way of simulating the fractural phenomenon of steel with the consideration of stress triaxiality, whereas the actual triaxial performance also depends on other factors such initial material imperfections and the direction of rolling [34].

5.2. FE results and discussions

The load–deflection responses and fractural phenomena of the specimens predicted by the FE models are compared with the test results as shown in Figs. 4–6. Good agreements are generally

observed between the FE predictions and test results, especially in terms of the trend of load dropping and regaining responses as well as the fractural patterns. The minor discrepancy may be caused by some test uncertainties which are difficult to be fully reflected by the FE model. For instance, in the actual test, it was difficult to fully fix the pin-supports in the axial direction due to slight unavoidable gaps in the hinges as well as in the adjacent connectors; however, the beam ends of the FE model were considered as pin-supported in an idealised manner with no movement allowed in the axial direction. This idealised pin support condition in the FE model can cause more significant compressive arching effect in the initial stage, which may explain the slightly higher initial resisting load of the FE predictions compared with the test results for some specimens. Possible variations of material properties could also lead to the discrepancy. Nevertheless, the proposed FE modelling strategy can well capture all the key stages of the specimens from initial column removal until final collapse. Importantly, the late-stage load resisting mechanism of specimen I-W, which was not recorded by the test, is revealed by the FE predictions.

It is observed that the two boundary conditions considered for the centre column of model I-W leads to similar load–deflection development trends, but different fractural performances/sequences are developed. When the lower part of the centre column was laterally constrained, leading to symmetrical performance of the model at the two sides of the column, the load–deflection response exhibits two distinct load peaks, corresponding to the initial fracture at the bottom flange of the beam and the final fracture of the whole section. It is noted that with limited regain of the resistance, the resisting load at the second peak is significantly lower than that in the first peak. When the constraint at the lower part of the centre column is removed, which is closer to the actual testing conditions, the bottom flange of the beam at the west side fractures first, and it is until this crack propagates significantly into the web of beam that the initiation of fracture is induced at the opposite side of the column, as shown in Fig. 12 (a). This phenomenon is generally in line with the test observations. Both the test result and FE prediction show limited regaining of the resisting load of specimen I-W, which indicates that the welded flange-welded web solution for beam-to-SHS column connections have unsatisfactory resistance picking up mechanism at catenary stage once initial fracture occurs.

For specimens I-WB and ST-WB, the FE results confirm that the resisting load can regain evidently after initial fracture of the bottom flange of the beam, and the regained load can exceed the initial peak for specimen ST-WB. The FE predictions also confirm that the initial fracture of ST-WB occurs earlier than that of the other two specimens. In order to explain this phenomenon, Fig. 12(b) gives the PEEQ contour of the three specimens at a series of deflections. At $\Delta = 103$ mm, model ST-WB shows high strain levels at multiple locations, including the external edge of the bottom flange of the beam, the toe of the weld access hole, and the bottom corner of the shear tab near the weld line, which indicates that these areas are more prone to initial fracture. Similar PEEQ contour patterns are found for the other two models, but with slightly lower strain levels. When Δ increases to 150 mm, fracture has been induced for specimen ST-WB, and the crack is initiated from one external edge of the bottom flange of the beam. For the other two specimens, however, no fracture has been induced at this deflection, although high strain levels have been developed at those critical regions. When Δ further increases to 200 mm, complete fracture of the bottom flange of the beam is induced for model ST-WB, whereas for model I-WB, two cracks are simultaneously developed near the weld access hole and the edge of the beam flange. For model I-W, which is a fully welded connection, initial fracture is developed near the weld access hole and then a
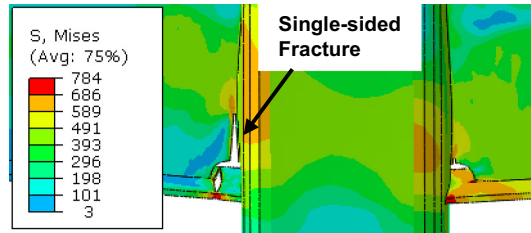
(a) Local fracture of model I-W
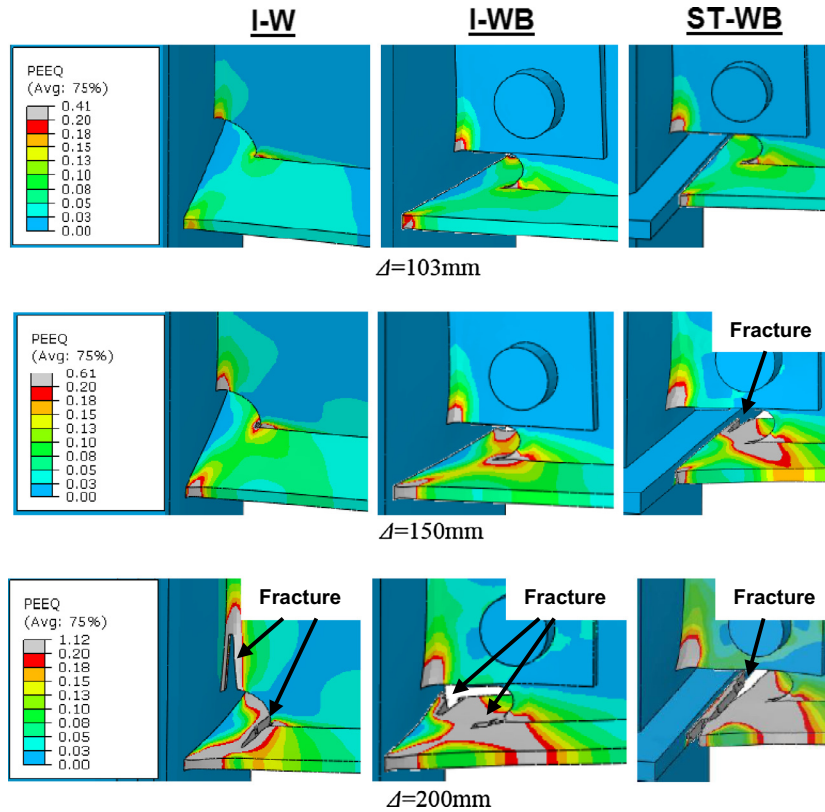
(b) Initiation and development of fracture
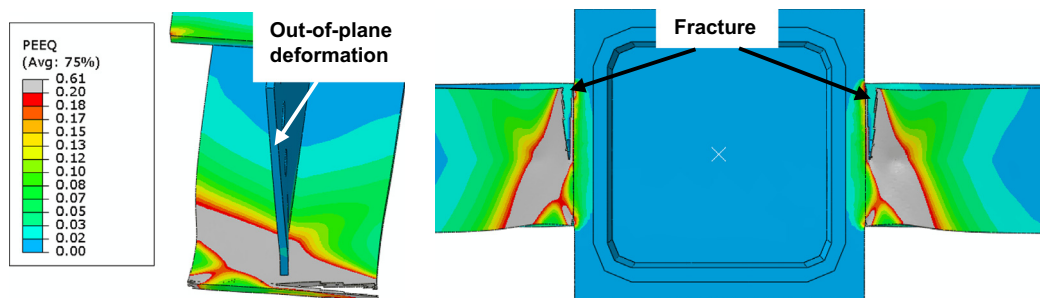
(c) Fracture pattern for specimen ST-WB

Fig. 12. Discussion of FE predictions.

second crack is induced at the beam web. All these fractural behaviour predicted by the FE models agrees very well with test observations.

It is of importance to find that for model ST-WB, the PEEQ pattern is distributed over the width of the beam flange in a non-symmetrical manner, and this could attribute to the initiation of fracture at only one edge of the bottom flange of the beam. The

non-symmetrical development of strain is probably due to the single-sided connection type between the beam web and the shear tab, which also causes out-of-plane deformation of the beam web, as shown in Fig. 12(c). This 'web twisting' effect can be more significant for model ST-WB than that for model I-WB because the 'coped length' (i.e. the length required for weld-access hole) of the steel beam is longer for the former case (in order to

accommodate more space for the short through diaphragms). As a result, the stress tends to be concentrated at one edge of the beam flange for model ST-WB, which causes earlier fracture at that area for the model. It is noted that as the web of model I-W is directly welded to the column wall with no out-of-plane eccentricity, a symmetrical strain pattern is developed over width of the beam flange. In this case, the strain demand is symmetrically shared by the beam flange, so the fracture development is also symmetrical. Therefore, from the perspective of initial fracture control, double-sided connections between the beam web and the column (e.g. double shear tabs) may be preferred, but further test evidence is desirable to confirm this.

Generally speaking, the rationality and effectiveness the FE modelling strategy, especially the way of addressing the complex issue of fracture simulation of the steel components, is verified. Whilst parametric studies are not within the scope of the current paper, the validated numerical model can form an important basis for the future studies towards more detailed design regulations of such beam-to-SHS column connections (or similar connections types).

6. Summary and conclusions

This paper has comprehensively discussed the progressive collapse resistance of practical beam-to-SHS column connections that are widely used in modern construction. The study commenced with three full scale tests on double-span systems subjected to a typical column loss scenario. The three specimens included welded flange-weld web connection with internal diaphragms (specimen I-W), welded flange-bolted web connection with internal diaphragms (specimen I-WB), and welded flange-bolted web connection with short through diaphragms (specimen ST-WB). The test results, including failure modes/sequences, load–deformation responses and stress conditions, were presented in detail, and the load transfer mechanism along the entire loading process was thoroughly discussed. Comprehensive finite element (FE) models were then established to enable further discussion of the test results. Good agreements were generally observed between the FE predictions and test results, especially in terms of the trend of load dropping and regaining responses as well as the fractural patterns.

Based on both experimental and numerical results, it can be mainly observed that all the three specimens exhibited satisfactory ductility supply, and they shared a similar level of maximum load resistance due to a similar mechanism of fracture initiation. The first peak load was achieved mainly in the flexural bending stage (with minor catenary action developed), where the load resistance could reach a level which corresponded to the full (or almost full) plastic bending resistance of the beam section. Specimen I-WB, which employed a typical welded flange-bolted web solution, showed the highest deformability against initial fracture at the bottom flange of the beam. When short through diaphragms were employed (i.e. specimen ST-WB), however, the ductility supply against initial fracture could be evidently decreased due to high stress levels developed at one edge of the beam flange, causing earlier fracture at this area. It was deduced that employing double-sided connections between the beam web and the column (e.g. double shear tabs) may improve the ductility supply. After initial fracture, limited load resistance was shown for specimen I-W which adopted fully welded connections, and marginal catenary action was developed due to quick propagation of the crack over the entire beam section. For the remaining two specimens adopting welded flange-bolted web connections, remarkable catenary action was developed after initial fracture, where the maximum axial force developed in the system could achieve more than half

of the fully yielded axial resistance of the beam section. The stress demand is well redistributed to the bolted shear tab connection and the top flange of the beam, where the successive fracture along the bolt line enabled further deformability of the specimens with significant picking up of the resisting load.

From a sudden column removal point of view, however, it was deduced from the energy balance principle that the regained static load resistance at the catenary stage could not promote a second equilibrium of the system. In other words, the internal energy stored within the deformed system could not balance the external work done by the applied load if it caused initial fracture of the bottom flange of the beam. Towards a simplified and conservative failure criterion for such connections in practical design, it may be preliminarily concluded that, when a sudden column loss scenario is considered, progressive collapse can be triggered upon the initial fracture of the bottom flange of the beam.

References

[1] Chan TM, Gardner L. Compressive resistance of hot-rolled elliptical hollow sections. Eng Struct 2008;30(2):522–32.
[2] Li L, Wang W, Chen YY, Lu Y. Effect of beam web bolt arrangement on catenary behaviour of moment connections. J Constr Steel Res 2015;104:22–36.
[3] Ellingwood BR. Mitigating risk from abnormal loads and progressive collapse. J Perform Constr Facil 2006;20(4):315–23.
[4] National Institute of Science and Technology (NIST). Final report on the collapse of the world trade center towers. NCSTAR 1, US Department of Commerce, Gaithersburg, Maryland; 2005.
[5] General Service Administration (GSA). Progressive collapse analysis and design guidelines for new federal office buildings and major modernization projects, Washington, DC; 2003.
[6] Department of Defense (DoD). Design of buildings to resist progressive collapse, unified facilities criteria, 4-023-03; 2009.
[7] Tsitos A. Experimental and numerical investigation of the progressive collapse of steel frames. State University of New York; 2010.
[8] Astaneh-Asl A, Jones B, Zhao Y. Progressive collapse resistance of steel building floors, UCB/CEE-STEEL-2001/03. University of California at Berkeley; 2001.
[9] Song BI, Giriunas KA, Sezen H. Progressive collapse testing and analysis of a steel frame building. J Constr Steel Res 2014;94:76–83.
[10] Sadek F, Main JA, Lew HS, et al. Testing and analysis of steel and concrete beam-column assemblies under a column removal scenario. J Struct Eng 2011;137(9):881–92.
[11] Karns J, Houghton D, Hong J, Kim, J. Behaviour of varied steel frame connection types subjected to air blast, debris impact, and/or post-blast progressive collapse load conditions. In: Proceedings of the 2009 structures congress, USA; 2009.
[12] Li L, Wang W, Chen YY, Lu Y. Experimental investigation of beam-to-tubular column moment connections under column removal scenario. J Constr Steel Res 2013;88:244–55.
[13] Lew H, Main J, Robert S, et al. Performance of steel moment connections under a column removal scenario. I: Experiments. J Struct Eng 2012;139(1):98–107.
[14] Lee C, Kim S, Lee K. Parallel axial-flexural hinge model for nonlinear dynamic progressive collapse analysis of welded steel moment frames. J Struct Eng 2010;136(2):165–73.
[15] Yang B, Tan KH. Experimental tests of different types of bolted steel beam–column joints under a central-column-removal scenario. Eng Struct 2013;54:112–30.
[16] Yang B, Tan KH. Robustness of bolted-angle connections against progressive collapse: mechanical modelling of bolted-angle connections under tension. Eng Struct 2013;57:153–68.
[17] Kuhlmann IU, Rölle L. Robust structures by joint ductility: COST C-26 Workshop, Prague; 2007.
[18] Rölle L, Kuhlmann U. Partial-strength and highly ductile steel and composite joints as robustness measure: Nordic Steel Construction Conference 2009, Malmo; 2009.
[19] Huang ZH, Shi SQ, Cai LP. Experimental analysis on strength and failure modes of wood beam–column connections. Front Struct Civ Eng 2014;8(3):260–9.
[20] Yu M, Zha XX, Ye JQ. The influence of joints and composite floor slabs on effective tying of steel structures in preventing progressive collapse. J Constr Steel Res 2009;66(3):442–51.

[21] Alashker Y, El-Tawil S, Sadek F. Progressive collapse resistance of steel-concrete composite floors. J Struct Eng 2010;136(10):1187–96.

[22] Fang C, Izzuddin BA, Elghazouli AY, Nethercot DA. Robustness of steel-composite building structures subject to localised fire. Fire Saf J 2011;46(6):348–63.

[23] Fang C, Izzuddin BA, Elghazouli AY, Nethercot DA. Simplified energy-based robustness assessment for steel-composite car parks under vehicle fire. Eng Struct 2013;49:719–32.

[24] Izzuddin BA, Vlassis AG, Elghazouli AY, Nethercot DA. Progressive collapse of multi-storey buildings due to sudden column loss – Part I: Simplified assessment framework. Eng Struct 2008;30(5):1308–18.

[25] Vlassis AG, Izzuddin BA, Elghazouli AY, Nethercot DA. Progressive collapse of multi-storey buildings due to sudden column loss – Part II: Application. Eng Struct 2008;30(5):1424–38.

[26] Luu NNH. Structural response of steel and composite building frames further to an impact leading to the loss of a column. PhD Thesis. Department of Civil Engineering, University of liege, Belgium; 2008.

[27] Fadden M, McCormick J. Finite element model of the cyclic bending behavior of hollow structural sections. J Constr Steel Res 2014;94:64–75.

[28] Ministry of Construction of China: Code for design of steel structures (50017-2003), Beijing; 2003.

[29] American Society for Testing and Materials (ASTM). Standard test methods and definitions for mechanical testing of steel products, ASTM Standard A370-02, Philadelphia, PA; 2002.

[30] Wang KQ, Fang C, Li GQ, Izzuddin BA. An analytical model for evaluating axial boundary stiffness of steel beam restrained by neighboring floor systems. Int J Steel Struct 2011;11(4):457–66.

[31] ABAQUS Analysis user's manual, ABAQUS Standard, Version 6.11; 2011.

[32] Yang B, Tan KH. Numerical analyses of steel beam–column joints subjected to catenary action. J Constr Steel Res 2012;70:1–11.

[33] Khandelwal K, El-Tawil S. Collapse behavior of steel special moment resisting frame connections. J Struct Eng 2007;133(5):646–55.

[34] El-Tawil S, Vidarsson E, Mikesell T, Kunnath SK. Inelastic behavior and design of steel panel zones. J Struct Eng 1999;125(2):183–93.